



Tuning the spin Hall effect of Pt from the moderately dirty to the superclean regime

Edurne Sagasta,¹ Yasutomo Omori,² Miren Isasa,¹ Martin Gradhand,³ Luis E. Hueso,^{1,4} Yasuhiro Niimi,^{2,5} YoshiChika Otani,^{2,6} and Fèlix Casanova^{1,4,*}

¹*CIC nanoGUNE, 20018 Donostia-San Sebastian, Basque Country, Spain*

²*Institute for Solid State Physics, University of Tokyo, Kashiwa, Chiba 277-8581, Japan*

³*H. H. Wills Physics Laboratory, University of Bristol, Bristol BS8 1TL, United Kingdom*

⁴*IKERBASQUE, Basque Foundation for Science, 48011 Bilbao, Basque Country, Spain*

⁵*Department of Physics, Graduate School of Science, Osaka University, 1-1 Machikaneyama, Toyonaka, Osaka 560-0043, Japan*

⁶*RIKEN-CEMS, 2-1 Hirosawa, Wako, Saitama 351-0198, Japan*

(Received 11 March 2016; revised manuscript received 26 July 2016; published 30 August 2016)

We systematically measure and analyze the spin diffusion length and the spin Hall effect in Pt with a wide range of conductivities using the spin absorption method in lateral spin valve devices. We observe a linear relation between the spin diffusion length and the conductivity, evidencing that the spin relaxation in Pt is governed by the Elliott-Yafet mechanism. We find a single intrinsic spin Hall conductivity ($\sigma_{\text{SH}}^{\text{int}} = 1600 \pm 150 \Omega^{-1} \text{cm}^{-1}$) for Pt in the full range studied which is in good agreement with theory. We have obtained the crossover between the moderately dirty and the superclean scaling regimes of the spin Hall effect by tuning the conductivity. This is equivalent to that obtained for the anomalous Hall effect. Our results explain the spread of the spin Hall angle values in the literature and find a route to maximize this important parameter.

DOI: [10.1103/PhysRevB.94.060412](https://doi.org/10.1103/PhysRevB.94.060412)

Spin-orbit interaction is an essential ingredient in solid state physics [1,2] that has been gaining interest in the last decade due to the advantages it offers to exploit the coupling between spin and orbital momentum of electrons in *spintronic* devices, leading to the emerging field of *spin orbitronics* [3]. The discovery of new charge-to-spin current conversion effects such as the spin Hall effect (SHE) [4–7], the Rashba-Edelstein effect (REE) [8–10], or the spin-momentum locking (SML) in topological insulators [11–13] is expanding the possibility to create and detect spin currents without using ferromagnets (FMs) or magnetic fields. For instance, magnetization switching of ferromagnetic elements has been recently achieved with torques arising from the SHE [14], the REE [15], or the SML [16], and new spin-dependent phenomena such as the spin Seebeck effect [17] or spin pumping [18] have been discovered by using the SHE to detect spin currents.

The SHE is thus the crucial effect behind this breakthrough. Although it was predicted theoretically by Dyakonov and Perel 45 years ago [1] and revisited by Hirsch in 1999 [4], it took a bit longer to observe the first direct experimental evidence in semiconductors [19] and metals [6,7,18]. The SHE in a nonmagnet basically shares the same origin as the anomalous Hall effect (AHE) in FMs: in both effects, the spin-orbit coupling generates the opposite deflection of the spin-up and spin-down electrons in a charge current, leading to a transverse spin current. This can be detected as a transverse voltage in the AHE because the intrinsic spin polarization in FMs gives rise to a net charge accumulation. On the other hand, the SHE creates a transverse pure spin current, making it more difficult to detect. The inverse spin Hall effect (ISHE) is the reciprocal effect, in which pure spin currents are converted into charge currents. The efficiency of these conversions is given by the spin Hall angle, θ_{SH} .

The mechanisms behind the SHE, which can be either intrinsic or extrinsic, were first studied in the framework of the AHE. The intrinsic contribution, first proposed by Karplus and Luttinger [20], relies on the spin-dependent band structure of the conductor, and the transverse displacement of the spin-up and spin-down electrons occurs in between scattering events. Skew scattering, proposed by Smit [21], is an extrinsic contribution where the spin-dependent scattering arises due to the effective spin-orbit coupling of impurities in the lattice. A phonon skew scattering [22,23] has recently been shown to contribute in metals such as Au [24]. Side jump, another extrinsic mechanism introduced by Berger [25], results in a spin-dependent sideways displacement upon repeated scattering.

In contrast to the AHE [22,26–28], a systematic experimental study of the different mechanisms contributing to the SHE for relevant materials is lacking. Finding routes to maximize the SHE is not possible as long as it remains unclear whether the dominant mechanism in a material is intrinsic or extrinsic. This issue has particularly been controversial in Pt, the prototypical SHE metal, although a consensus that the intrinsic contribution is the dominant one is emerging [24,29,30]. Nevertheless, there is still a significant spread in the θ_{SH} values of Pt among different groups and techniques [5,31,32]. The spin-memory loss explained by Rojas-Sánchez *et al.* [31] is one of the causes for this, as well as the wide range of spin diffusion lengths λ_{Pt} used by different groups [32]. A proper understanding of the SHE in order to correctly quantify and tune θ_{SH} in Pt is thus of utmost importance.

In this Rapid Communication, we experimentally study the spin diffusion length and the SHE in Pt with a broad range of longitudinal conductivities (σ_{Pt}). The linear relation obtained between λ_{Pt} and σ_{Pt} evidences that the spin relaxation in Pt is governed by the Elliott-Yafet mechanism. We obtain a single intrinsic spin Hall conductivity for the full range studied, in good agreement with theoretical predictions. In addition, we identify slightly different skew scattering angles for Pt deposited with different techniques. By tuning the SHE with

*Corresponding author: f.casanova@nanogune.eu

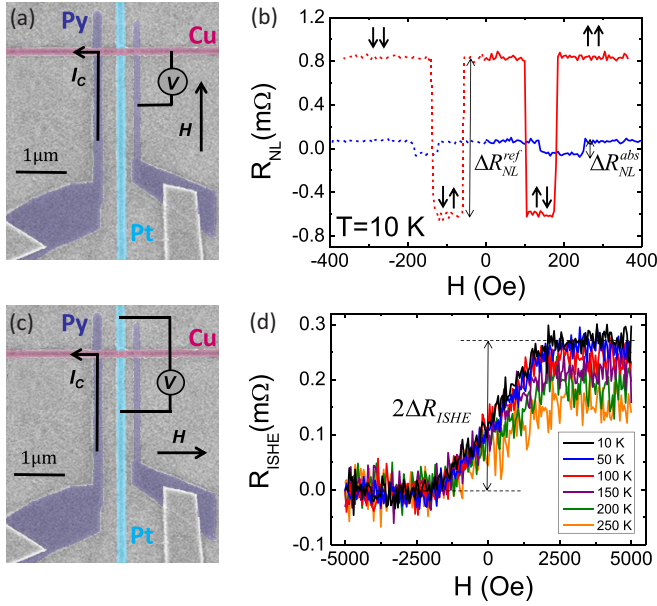


FIG. 1. (a) Scanning electron microscopy (SEM) image of a Py/Cu lateral spin valve with a Pt wire between the two Py electrodes. The nonlocal measurement configuration, the direction of the applied magnetic field (H), and the materials (Py, Cu, and Pt) are shown. (b) Nonlocal resistance as a function of H measured at $I_C = 100 \mu\text{A}$ and 10 K in the configuration shown in (a) for a Py/Cu lateral spin valve with (blue line) and without (red line) a Pt wire in between the Py electrodes. The solid (dashed) line corresponds to the increasing (decreasing) magnetic field. The reference spin signal ($\Delta R_{NL}^{\text{ref}}$) and the spin signal with Pt absorption ($\Delta R_{NL}^{\text{abs}}$) are tagged. (c) SEM image of the same device used now to measure the ISHE. The materials, the direction of H , and the measurement configuration for ISHE are shown. (d) ISHE resistance as a function of H measured at $I_C = 100 \mu\text{A}$ and different temperatures in the configuration shown in (c). The curves have been shifted for clarity. The ISHE signal ($2\Delta R_{ISHE}$) for 10 K is tagged. Images and data correspond to device S2.

σ_{Pt} , we can thus observe the crossover from a moderately dirty regime, where the intrinsic contribution is dominant, to the superclean regime, dominated by extrinsic effects. A similar crossover has been discussed in the AHE [27,28], but has never been observed experimentally in any spin Hall system before. This result clearly elucidates the detailed mechanisms of the SHE in its prototypical metal.

We used the spin absorption method in lateral spin valve devices, which enables us to quantitatively derive both the spin diffusion length (via the spin absorption) and the spin Hall angle (via the ISHE) of Pt in the same device [7,24,29,33–36]. To this end, eight devices were fabricated on top of a $\text{SiO}_2(150 \text{ nm})/\text{Si}$ substrate by using multiple-step e-beam lithography, subsequent metal deposition, and lift-off. Each device contains two Py/Cu lateral spin valves, both with the same Py interelectrode distance $L \sim 630 \text{ nm}$, but one of them with a Pt wire in between the electrodes, as shown in Fig. 1(a). First, each pair of Py electrodes was patterned with different widths, $\sim 100 \text{ nm}$ and $\sim 170 \text{ nm}$, in order to obtain different switching magnetic fields, and 35 nm of Py were e-beam evaporated. During the second step, a $\sim 130\text{-nm}$ -wide and 20-nm-thick Pt wire was deposited by e-beam evaporation (base pressure $\leq 1 \times 10^{-8}$ torr, rate $0.1\text{--}2 \text{ \AA/s}$, substrate temperature $5\text{--}7 \text{ }^\circ\text{C}$) in half of the devices (E1, E2, E3, E4) and by magnetron sputtering (base pressure 1×10^{-7} to 1×10^{-8} torr, power 80 W, Ar pressure 3×10^{-3} torr, rate 1.3 \AA/s , substrate temperature $25 \text{ }^\circ\text{C}$) in the other half (S1, S2, S3, S4). The different Pt wires cover a broad range of resistivities, with evaporated ones having a smaller residual resistivity $\rho_{Pt,0}$ than sputtered ones (see Table I) [37]. In the third lithography step, a $\sim 150\text{-nm}$ -wide channel was patterned and a 100-nm-thick Cu was thermally evaporated. In order to have highly transparent Py/Cu and Pt/Cu interfaces, the surfaces of the Py and Pt wires were cleaned via Ar-ion beam etching before the Cu deposition. All nonlocal transport measurements described below were carried out in a liquid-He cryostat (applying an external magnetic field H and varying temperature T) using a “dc reversal” technique [39].

When a spin-polarized current is injected from one Py electrode, as shown in Fig. 1(a), a spin accumulation is created at the Py/Cu interface. This spin accumulation diffuses along both sides of the Cu channel, creating a pure spin current which is detected as a voltage by the second Py electrode. Normalizing the measured voltage to the injected current I_C , the nonlocal resistance R_{NL} is defined. This value changes sign when the relative magnetization of the two Py electrodes is switched from parallel to antiparallel by sweeping H . The change from positive to negative R_{NL} is defined as the spin signal ΔR_{NL} . The reference value $\Delta R_{NL}^{\text{ref}}$ is measured without the Pt wire [see the red line in Fig. 1(b)]. If a Pt wire is inserted between the Py electrodes, a part of the spin current diffusing along the Cu channel will be absorbed into the Pt and a smaller spin signal $\Delta R_{NL}^{\text{abs}}$ will be measured in the Py

TABLE I. Intrinsic spin Hall conductivity (σ_{SH}^{int}) and skew scattering angle (α_{ss}) extracted from the individual fittings of each device used in this work. Residual resistivity ($\rho_{Pt,0}$), the spin diffusion length (λ_{Pt}), and the spin Hall angle (θ_{SH}) at 10 K are also included.

Device	$\rho_{Pt,0}(\mu\Omega \text{ cm})$	$\lambda_{Pt}(\text{nm})$	$\theta_{SH}(\%)$	$\sigma_{SH}^{\text{int}}(\Omega^{-1} \text{ cm}^{-1})$	$\alpha_{ss}(\%)$
E1	6.66	10.1 ± 0.1	2.1 ± 0.7	1480 ± 110	1.2 ± 0.2
E2	6.66	10.1 ± 0.1	1.7 ± 0.4	1780 ± 95	0.7 ± 0.2
E3	9.42	6.7 ± 0.1	2.2 ± 0.2	1750 ± 360	0.4 ± 0.5
E4	10.12	6.5 ± 0.1	2.2 ± 0.3	1910 ± 700	0.1 ± 0.9
S1	44.19	0.75 ± 0.03	8.5 ± 1.3	1525 ± 220	2.1 ± 1.3
S2	44.19	0.75 ± 0.03	7.4 ± 0.7	1280 ± 140	2.0 ± 0.9
S3	24.96	3.43 ± 0.05	5.3 ± 0.6	1435 ± 390	1.9 ± 1.3
S4	56.25	0.59 ± 0.01	10.7 ± 1.0	1770 ± 760	1.6 ± 5.2

detector, as shown by the blue line in Fig. 1(b). The spin diffusion length of Pt is obtained from the ratio of both spin signals, which from the one-dimensional spin diffusion model for transparent interfaces is expressed as

$$\frac{\Delta R_{\text{NL}}^{\text{abs}}}{\Delta R_{\text{NL}}^{\text{ref}}} = \frac{2Q_{\text{Pt}}[\sinh(\frac{L}{\lambda_{\text{Cu}}}) + 2Q_{\text{Py}}e^{L/\lambda_{\text{Cu}}} + 2Q_{\text{Py}}^2e^{L/\lambda_{\text{Cu}}}]}{\cosh(\frac{L}{\lambda_{\text{Cu}}}) - \cosh(\frac{L-2d}{\lambda_{\text{Cu}}}) + 2Q_{\text{Py}}\sinh(\frac{d}{\lambda_{\text{Cu}}})e^{(L-d)/\lambda_{\text{Cu}}} + 2Q_{\text{Pt}}\sinh(\frac{L}{\lambda_{\text{Cu}}}) + 4Q_{\text{Py}}Q_{\text{Pt}}e^{L/\lambda_{\text{Cu}}} + 2Q_{\text{Py}}e^{d/\lambda_{\text{Cu}}}\sinh(\frac{L-d}{\lambda_{\text{Cu}}}) + 2Q_{\text{Py}}^2e^{L/\lambda_{\text{Cu}}} + 4Q_{\text{Py}}^2Q_{\text{Pt}}e^{L/\lambda_{\text{Cu}}}}, \quad (1)$$

where $Q_{\text{Py(Pt)}} = R_{\text{Py(Pt)}}/R_{\text{Cu}}$, being $R_{\text{Cu}} = \lambda_{\text{Cu}}\rho_{\text{Cu}}/w_{\text{Cu}}t_{\text{Cu}}$, $R_{\text{Py}} = \lambda_{\text{Py}}\rho_{\text{Py}}/w_{\text{Cu}}w_{\text{Py}}(1 - \alpha_{\text{Py}}^2)$, and $R_{\text{Pt}} = \lambda_{\text{Pt}}\rho_{\text{Pt}}/w_{\text{Cu}}w_{\text{Pt}}\tanh(t_{\text{Pt}}/\lambda_{\text{Pt}})$ the spin resistances of the Cu channel, Py electrodes, and Pt wire, respectively. Here, $\rho_{\text{Cu,Py,Pt}}$, $\lambda_{\text{Cu,Py,Pt}}$, $w_{\text{Cu,Py,Pt}}$, and $t_{\text{Cu,Pt}}$ are the resistivities, spin diffusion lengths, widths, and thicknesses, respectively. The Pt resistivities for all devices are plotted as a function of temperature in Fig. 2(a). α_{Py} is the spin polarization of Py. L is the distance between the two Py electrodes, whereas d is the distance between the Py injector and the Pt wire. Since R_{Cu} and R_{Py} values are well known from our previous work [40,41], λ_{Pt} can be obtained from Eq. (1) [42]. By repeating the measurement shown in Fig. 1(b) at different temperatures and devices, λ_{Pt} as a function of temperature was obtained for all devices [Fig. 2(b)].

The spin diffusion lengths are plotted in Fig. 2(c) as a function of the conductivity of Pt ($\sigma_{\text{Pt}} = \rho_{\text{Pt}}^{-1}$), which changes from device to device and with temperature. The linear dependence between λ_{Pt} and σ_{Pt} confirms that Elliott-Yafet [46,47] is the main spin relaxation mechanism in Pt, as also observed recently using other experimental techniques [30,48]. From our data, we obtain a slope of $(0.61 \pm 0.02) \times 10^{-15} \Omega \text{ m}^2$, which is in excellent agreement with a recent theoretical prediction $[(0.63 \pm 0.02) \times 10^{-15} \Omega \text{ m}^2]$ from first-principles scattering theory combined with temperature-induced disorder [49]. The spin-flip probability for Pt can be calculated from the slope [50], yielding $a_{\text{sf}} = 0.57$, a large value expected from the strong spin-orbit coupling in Pt [52]. For comparison, a good

spin transport metal such as Cu has $a_{\text{sf}} = 4.9\text{--}11.0 \times 10^{-4}$ [40,53].

Next, we measured the ISHE in Pt for the eight devices by changing the measurement configuration to the one described in Fig. 1(c). As in the previous configuration, the pure spin current injected from the Py electrode diffuses along the Cu channel and is partly absorbed by the Pt wire. In this Pt wire, due to the ISHE, a charge current perpendicular to both the spin current direction and spin polarization is created and, thus, a voltage drop is generated along the Pt wire. The measured voltage normalized to the injected current I_C yields the ISHE resistance R_{ISHE} . By switching the orientation of the magnetic field, the opposite R_{ISHE} is obtained, since the Py magnetization is inverted as well as the orientation of the spin polarization. The difference of the two R_{ISHE} values is twice the ISHE signal: $2\Delta R_{\text{ISHE}}$. Figure 1(d) shows the measured R_{ISHE} at different temperatures for one device. We repeated these measurements for each device.

ΔR_{ISHE} is related to the spin Hall conductivity σ_{SH} by [54]

$$\sigma_{\text{SH}} = \sigma_{\text{Pt}}^2 \frac{w_{\text{Pt}}}{x_{\text{Pt}}} \left(\frac{I_C}{I_s} \right) \Delta R_{\text{ISHE}}, \quad (2)$$

where x_{Pt} is the shunting factor which takes into account the current in the Pt that is shunted through the Cu and is obtained from numerical calculations using a finite elements method [56]. I_s is the effective spin current that contributes to the ISHE in Pt and is given by [24]

$$\frac{I_s}{I_C} = \frac{\lambda_{\text{Pt}}(1 - e^{-t_{\text{Pt}}/\lambda_{\text{Pt}}})^2}{t_{\text{Pt}}(1 - e^{-2t_{\text{Pt}}/\lambda_{\text{Pt}}})} \times \frac{2\alpha_{\text{Py}}[Q_{\text{Py}}\sinh(\frac{L-d}{\lambda_{\text{Cu}}}) + Q_{\text{Py}}^2e^{(L-d)/\lambda_{\text{Cu}}}]}{\cosh(\frac{L}{\lambda_{\text{Cu}}}) - \cosh(\frac{L-2d}{\lambda_{\text{Cu}}}) + 2Q_{\text{Py}}\sinh(\frac{d}{\lambda_{\text{Cu}}})e^{(L-d)/\lambda_{\text{Cu}}} + 2Q_{\text{Pt}}\sinh(\frac{L}{\lambda_{\text{Cu}}}) + 4Q_{\text{Py}}Q_{\text{Pt}}e^{L/\lambda_{\text{Cu}}} + 2Q_{\text{Py}}e^{d/\lambda_{\text{Cu}}}\sinh(\frac{L-d}{\lambda_{\text{Cu}}}) + 2Q_{\text{Py}}^2e^{L/\lambda_{\text{Cu}}} + 4Q_{\text{Py}}^2Q_{\text{Pt}}e^{L/\lambda_{\text{Cu}}}}. \quad (3)$$

The spin Hall resistivity ρ_{SH} is related to σ_{SH} as $\rho_{\text{SH}} = -\sigma_{\text{SH}}/(\sigma_{\text{Pt}}^2 + \sigma_{\text{SH}}^2) \approx -\sigma_{\text{SH}}/\sigma_{\text{Pt}}^2$. The spin Hall angle θ_{SH} can be written in terms of either σ_{SH} or ρ_{SH} : $\theta_{\text{SH}} = \sigma_{\text{SH}}/\sigma_{\text{Pt}} = -\rho_{\text{SH}}/\rho_{\text{Pt}}$. In order to analyze how the intrinsic and extrinsic mechanisms contribute to the SHE in each device, we will analyze the dependence of ρ_{SH} on the longitudinal resistivity ρ_{Pt} . As the side jump mechanism arises only in materials with high impurity concentrations [5,57,58], this contribution is negligible in our high purity Pt. The same holds for the phonon skew scattering, due to its small effect in Pt [24]. Therefore, based on the scaling relation introduced by Tian *et al.* [22], this leads us to

$$-\rho_{\text{SH}} = \alpha_{\text{ss}}\rho_{\text{Pt},0} + \sigma_{\text{SH}}^{\text{int}}\rho_{\text{Pt}}^2. \quad (4)$$

By plotting $-\rho_{\text{SH}}$ against ρ_{Pt}^2 , we are able to fit a linear function with a slope that corresponds to the intrinsic contribution, $\sigma_{\text{SH}}^{\text{int}}$, and the intercept divided by $\rho_{\text{Pt},0}$ defines the skew scattering angle α_{ss} . Figure 3 shows the data for all devices and the corresponding linear fits. The values extracted from the eight devices are collected in Table I.

Interestingly, the data in Table I reveals that the extracted intrinsic spin Hall conductivities for all the devices are very close to each other, especially when taking into account the different resistivities and θ_{SH} in each device. We obtain an average value of $\sigma_{\text{SH}}^{\text{int}} = 1600 \pm 150 \Omega^{-1}\text{cm}^{-1}$ for Pt, indicating that the intrinsic contribution of the spin Hall conductivity is a constant within a 10% dispersion. This is a remarkable finding, which is in excellent agreement with theoretical values of $1300 \Omega^{-1}\text{cm}^{-1}$ [59] and $1600 \Omega^{-1}\text{cm}^{-1}$

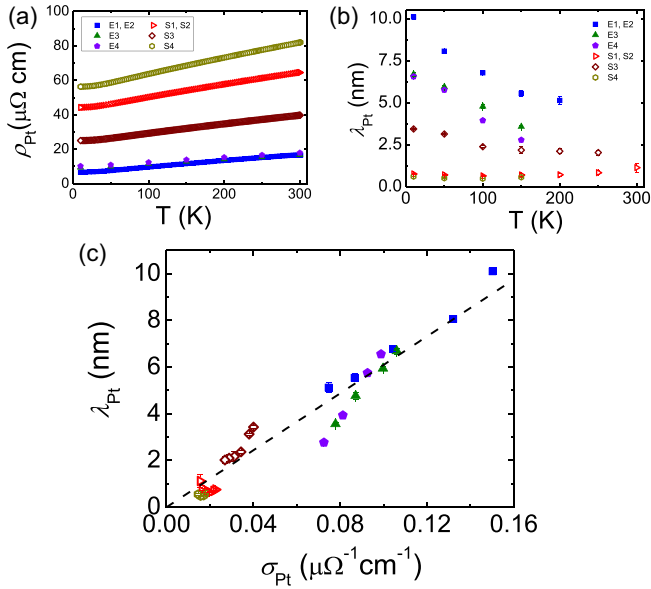


FIG. 2. (a) Resistivity and (b) spin diffusion length of Pt as a function of temperature for all devices. Error bars are included. (c) Spin diffusion length of Pt as a function of longitudinal conductivity for all devices. Error bars are included. The black dashed line is a linear fitting of the experimental data. Since devices E1 and E2 (S1 and S2) were fabricated in the same chip, Pt was evaporated (sputtered) in the same deposition, hence it is assumed that E1 and E2 (S1 and S2) have the same ρ_{Pt} and λ_{Pt} .

[60] obtained with different approaches. The predicted decrease of the intrinsic spin Hall conductivity of Pt at higher resistivities by Tanaka *et al.* [59] lies outside our studied range. A recent experimental study employing the spin torque ferromagnetic resonance technique reports a lower bound of $\sigma_{\text{SH}}^{\text{int}} = 2950 \pm 100 \Omega^{-1} \text{cm}^{-1}$ for Pt [30], much higher than ours and the theoretical predictions.

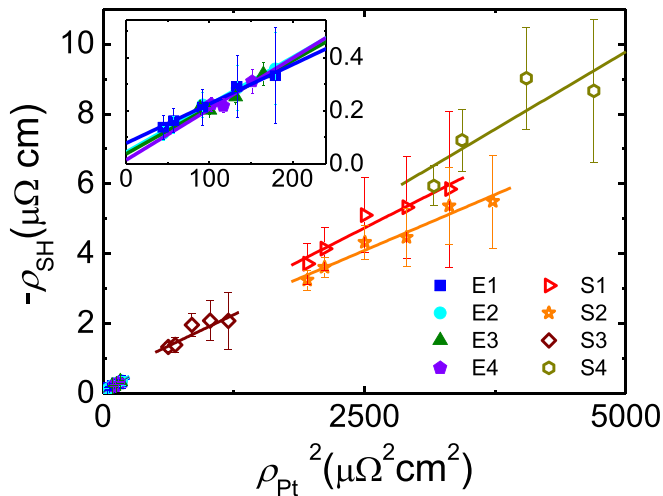


FIG. 3. Spin Hall resistivity as a function of the square of the longitudinal resistivity of Pt for all devices. Error bars are included. Solid lines correspond to the fit of the data to Eq. (4). Inset: Zoom of the previous plot showing the data of the devices with evaporated Pt.

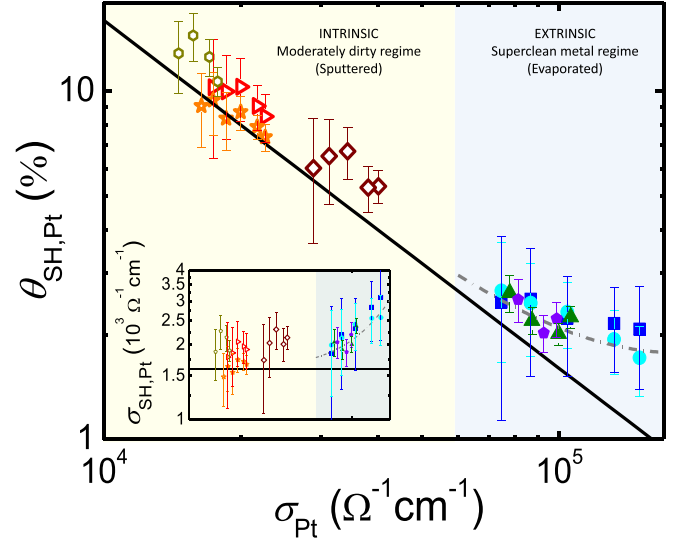


FIG. 4. Spin Hall angle as a function of the longitudinal conductivity of Pt for all devices. Error bars are included. The regions with different scaling regimes are indicated. The black solid line corresponds to the intrinsic contribution of the spin Hall angle $\theta_{\text{SH}}^{\text{int}} = \sigma_{\text{SH}}^{\text{int}}/\sigma_{\text{Pt}}$, using $\sigma_{\text{SH}}^{\text{int}} = 1600 \Omega^{-1} \text{cm}^{-1}$. The gray dashed line in the superclean region corresponds to the total spin Hall angle calculated with both intrinsic and skew scattering contributions, using the average value $\alpha_{\text{ss}}(\%) = 0.6$ obtained for this region. Inset: Same data plotted as spin Hall conductivity. The scale of the horizontal axis is the same as in the main panel.

The skew scattering angle yields similar values for all the devices deposited with the same technique, but slightly different for each deposition type. The observation is reasonable as this extrinsic contribution depends directly on the kind of defects in the Pt. Sputtered and evaporated Pt have different grain sizes and, moreover, the deposition in different chambers gives rise to the presence of different impurities, hence explaining the different skew scattering contribution in each type of Pt.

In contrast to Ref. [22], we cannot plot a universal curve for all devices using Eq. (4) because the extrinsic contribution differs from the evaporated to the sputtered Pt. Nevertheless, we can still plot θ_{SH} (and σ_{SH}) as a function of σ_{Pt} (see Fig. 4 and inset) in order to compare the relative weight of the different contributions in an analogy to the different scaling regimes observed in the AHE [22,26–28].

The spin Hall angle for evaporated and sputtered devices scale in a very different way with σ_{Pt} , as can be seen in Fig. 4. θ_{SH} for sputtered devices, with highest resistivity, shows the same trend expected from the intrinsic contribution ($\theta_{\text{SH}}^{\text{int}} = \sigma_{\text{SH}}^{\text{int}}/\sigma_{\text{Pt}}$, black solid line), and the total experimental θ_{SH} nearly merges into the intrinsic value (the small difference is given by the minor contribution of the skew scattering). This region dominated by the intrinsic scaling regime thus corresponds to the moderately dirty region, similarly to what is observed in the AHE [27,28]. In contrast, in the lower resistivity region, the intrinsic contribution cannot explain the values of the experimental data, even the trend. Nevertheless, by adding the corresponding extrinsic contribution for this region to the diminishing intrinsic one, we obtain the gray

dashed line that matches perfectly with our data. This region is thus representing a clean metal, where the skew scattering dominates the scaling. Consequently, we observe the crossover from the intrinsic moderately dirty regime to the extrinsic superclean regime for the SHE, demonstrating a perfect correspondence with the AHE [27,28].

To conclude, we experimentally show for Pt a general scaling of the SHE. We demonstrate that $\sigma_{\text{SH}}^{\text{int}}$ is constant in Pt and this allows us to move from an intrinsic to an extrinsic regime when decreasing the resistivity from a moderately dirty to a clean metal. It is a further step towards a complete understanding of the SHE phenomenon, which can be extrapolated to other materials with strong spin-orbit coupling showing the SHE. Interestingly, our experimental results evidence that the variation of the Pt resistivity among different groups is one of the main reasons for the spread of θ_{SH} values in literature. Indeed, we are able to tune θ_{SH} from $\sim 2\%$ to 14% by varying the Pt resistivity from ~ 7 to $70 \mu\Omega \text{ cm}$. A very important consequence is that we show a clear path to enhance θ_{SH} by simply increasing the resistivity of any material with a dominant

intrinsic contribution to the SHE. Additionally, we confirmed that Elliott-Yafet is the main spin relaxation mechanism in Pt.

The authors thank Dr. P. Laczkowski for fruitful discussions. This work is supported by the European Research Council (Grant No. 257654-SPINTROS), by the Spanish MINECO under Projects No. MAT2012-37638 and No. MAT2015-65159-R, and by the Japanese JSPS Grant-in-Aid for Scientific Research on Innovative Area, “Nano Spin Conversion Science” (Grant No. 26103002). M.G. acknowledges financial support from the Leverhulme Trust via an Early Career Research Fellowship (ECF-2013-538). E.S. and M.I. thank the Spanish MEC and the Basque Government, respectively, for a Ph.D. fellowship (Grants No. FPU14/03102 and No. BFI-2011-106). Y.O. acknowledges financial support from JSPS through “Research program for Young Scientists” (Grant No. 15J08073) and “Program for Leading Graduate Schools (MERIT).”

E.S., Y.O., and M.I. contributed equally to this work.

-
- [1] M. I. Dyakonov and V. I. Perel, *Phys. Lett. A* **35**, 459 (1971).
 [2] Y. A. Bychkov and E. I. Rashba, *Pis'ma Zh. Eksp. Teor. Fiz.* **39**, 66 (1984) [*JETP Lett.* **39**, 78 (1984)].
 [3] T. Kuschel and G. Reiss, *Nat. Nanotechnol.* **10**, 22 (2015).
 [4] J. E. Hirsch, *Phys. Rev. Lett.* **83**, 1834 (1999).
 [5] A. Hoffmann, *IEEE Trans. Magn.* **49**, 5172 (2013); J. Sinova, S. O. Valenzuela, J. Wunderlich, C. H. Back, and T. Jungwirth, *Rev. Mod. Phys.* **87**, 1213 (2015).
 [6] S. O. Valenzuela and M. Tinkham, *Nature (London)* **442**, 176 (2006).
 [7] T. Kimura, Y. Otani, T. Sato, S. Takahashi, and S. Maekawa, *Phys. Rev. Lett.* **98**, 156601 (2007).
 [8] V. M. Edelstein, *Solid State Commun.* **73**, 233 (1990); K. Shen, G. Vignale, and R. Raimondi, *Phys. Rev. Lett.* **112**, 096601 (2014).
 [9] J. C. Rojas Sánchez, L. Vila, G. Desfonds, S. Gambarelli, J. P. Attané, J. M. De Teresa, C. Magén, and A. Fert, *Nat. Commun.* **4**, 2944 (2013).
 [10] M. Isasa, M. C. Martínez-Velarte, E. Villamor, C. Magén, L. Morellón, J. M. De Teresa, M. R. Ibarra, G. Vignale, E. V. Chulkov, E. E. Krasovskii, L. E. Hueso, and F. Casanova, *Phys. Rev. B* **93**, 014420 (2016).
 [11] C. H. Li, O. M. J. van't Erve, J. T. Robinson, Y. Liu, L. Li, and B. T. Jonker, *Nat. Nanotechnol.* **9**, 218 (2014).
 [12] A. Dankert, J. Geurs, M. V. Kamalakar, S. Charpentier, and S. P. Dash, *Nano Lett.* **15**, 7976 (2015).
 [13] Y. Shiomi, K. Nomura, Y. Kajiwara, K. Eto, M. Novak, K. Segawa, Y. Ando, and E. Saitoh, *Phys. Rev. Lett.* **113**, 196601 (2014).
 [14] L. Liu, C.-F. Pai, Y. Li, H. W. Tseng, D. C. Ralph, and R. A. Buhrman, *Science* **336**, 555 (2012).
 [15] I. M. Miron, K. Garello, G. Gaudin, P.-J. Zermatten, M. V. Costache, S. Auffret, S. Bandiera, B. Rodmacq, A. Schuhl, and P. Gambardella, *Nature (London)* **476**, 189 (2011); K. Garello, I. M. Miron, C. O. Avci, F. Freimuth, Y. Mokrousov, S. Blügel, S. Auffret, O. Boulle, G. Gaudin, and P. Gambardella, *Nat. Nanotechnol.* **8**, 587 (2013).
 [16] A. R. Mellnik, J. S. Lee, A. Richadella, J. L. Grab, P. J. Mintun, M. H. Fisher, A. Vaezi, A. Manchon, E. A. Kim, N. Samarth, and D. C. Ralph, *Nature (London)* **511**, 449 (2014).
 [17] K. Uchida, J. Xiao, H. Adachi, J. Ohe, S. Takahashi, J. Ieda, T. Ota, Y. Kajiwara, H. Umezawa, H. Kawai, G. E. W. Bauer, S. Maekawa, and E. Saitoh, *Nat. Mater.* **9**, 894 (2010).
 [18] E. Saitoh, M. Ueda, H. Mikajima, and G. Tatara, *Appl. Phys. Lett.* **88**, 182509 (2006).
 [19] Y. K. Kato, R. C. Myers, A. C. Gossard, and D. D. Awschalom, *Science* **306**, 1910 (2004).
 [20] R. Karplus and J. M. Luttinger, *Phys. Rev.* **95**, 1154 (1954).
 [21] J. Smit, *Physica* **24**, 39 (1958).
 [22] Y. Tian, L. Ye, and X. Jin, *Phys. Rev. Lett.* **103**, 087206 (2009).
 [23] C. Gorini, U. Eckern, and R. Raimondi, *Phys. Rev. Lett.* **115**, 076602 (2015).
 [24] M. Isasa, E. Villamor, L. E. Hueso, M. Gradhand, and F. Casanova, *Phys. Rev. B* **91**, 024402 (2015); **92**, 019905(E) (2015).
 [25] L. Berger, *Phys. Rev. B* **2**, 4559 (1970).
 [26] S. Onoda, N. Sugimoto, and N. Nagaosa, *Phys. Rev. Lett.* **97**, 126602 (2006).
 [27] S. Onoda, N. Sugimoto, and N. Nagaosa, *Phys. Rev. B* **77**, 165103 (2008).
 [28] S. Sangiao, L. Morellón, G. Simon, J. M. De Teresa, J. A. Pardo, J. Arbiol, and M. R. Ibarra, *Phys. Rev. B* **79**, 014431 (2009).
 [29] M. Morota, Y. Niimi, K. Ohnishi, D. H. Wei, T. Tanaka, H. Kontani, T. Kimura, and Y. Otani, *Phys. Rev. B* **83**, 174405 (2011).
 [30] M.-H. Nguyen, D. C. Ralph, and R. A. Buhrman, *Phys. Rev. Lett.* **116**, 126601 (2016).
 [31] J.-C. Rojas-Sánchez, N. Reyren, P. Laczkowski, W. Savero, J.-P. Attané, C. Deranlot, M. Jamet, J.-M. George, L. Vila, and H. Jaffrès, *Phys. Rev. Lett.* **112**, 106602 (2014).
 [32] L. Liu, R. A. Buhrman, and D. C. Ralph, *arXiv:1111.3702*.
 [33] Y. Niimi, H. Suzuki, Y. Kawanishi, Y. Omori, T. Valet, A. Fert, and Y. Otani, *Phys. Rev. B* **89**, 054401 (2014).

- [34] Y. Niimi, Y. Kawanishi, D. H. Wei, C. Deranlot, H. X. Yang, M. Chshiev, T. Valet, A. Fert, and Y. Otani, *Phys. Rev. Lett.* **109**, 156602 (2012).
- [35] Y. Niimi, M. Morota, D. H. Wei, C. Deranlot, M. Basletic, A. Hamzic, A. Fert, and Y. Otani, *Phys. Rev. Lett.* **106**, 126601 (2011).
- [36] P. Laczkowski, J.-C. Rojas-Sánchez, W. Saverio-Torres, H. Jaffrès, N. Reyren, C. Deranlot, L. Notin, C. Beigné, A. Marty, J.-P. Attané, L. Vila, J.-M. George, and A. Fert, *Appl. Phys. Lett.* **104**, 142403 (2014).
- [37] This difference is expected because sputtering is performed under higher pressure, leading to smaller grain sizes [38] and thus higher residual resistivity. The tuning of resistivity within the same technique is achieved by small variations in the base pressure (sputtering) or in the deposition rate (evaporation), although due to the delicate nature of nanostructures, the same deposition conditions can also give rise to slightly different resistivities.
- [38] K. S. Sree Harsha, *Principles of Physical Vapor Deposition of Thin Films*, 1st ed. (Elsevier, New York, 2006).
- [39] M. Erekhinsky, A. Sharoni, F. Casanova, and I. K. Schuller, *Appl. Phys. Lett.* **96**, 022513 (2010); M. Erekhinsky, F. Casanova, I. K. Schuller, and A. Sharoni, *ibid.* **100**, 212401 (2012).
- [40] E. Villamor, M. Isasa, L. E. Hueso and F. Casanova, *Phys. Rev. B* **87**, 094417 (2013).
- [41] E. Villamor, M. Isasa, L. E. Hueso and F. Casanova, *Phys. Rev. B* **88**, 184411 (2013).
- [42] As the width of our Pt wires is much smaller than λ_{Cu} [40], the correction to Eq. (1) recently introduced by Laczkowski *et al.* [43] that takes into account the spin accumulation profile under the absorber is not necessary. Although spin-memory loss plays a role in methods involving Pt/FM bilayers [31], it is most likely less significant, and difficult to unambiguously determine, in the spin absorption technique [44,45].
- [43] P. Laczkowski, H. Jaffrès, W. Saverio-Torres, J.-C. Rojas-Sánchez, Y. Fu, N. Reyren, C. Deranlot, L. Notin, C. Beigné, J.-P. Attané, L. Vila, J.-M. George, and A. Marty, *Phys. Rev. B* **92**, 214405 (2015).
- [44] Y. Niimi and Y. Otani, *Rep. Prog. Phys.* **78**, 124501 (2015).
- [45] M. Isasa, Spin orbitronics in metals, Ph.D. thesis, University of the Basque Country, 2015, <http://www.nanogune.eu/publications/p-1-phd-theses/2016?idThesis=27>.
- [46] R. J. Elliott, *Phys. Rev.* **96**, 266 (1954).
- [47] Y. Yafet, *Solid State Phys.* **14**, 1 (1963).
- [48] H. Y. T. Nguyen, W. P. Pratt, Jr., and J. Bass, *J. Magn. Magn. Mater.* **361**, 30 (2014).
- [49] Y. Liu, Z. Yuan, R. J. H. Wesselink, A. A. Starikov, M. van Schilfhaarde, and P. J. Kelly, *Phys. Rev. B* **91**, 220405(R) (2015).
- [50] Taking into account that the spin-flip probability is given by $a_{sf} = \tau_e/\tau_{sf} = 1/3(l_e/\lambda_{\text{Pt}})^2$ being τ_e and τ_{sf} the momentum scattering time and spin relaxation time, respectively, and that the mean free path for Pt can be calculated as $l_e \approx 8 \times 10^{-16}[\Omega \text{ m}^2]/\rho_{\text{Pt}}$ [51], we obtain $a_{sf} = 0.57$.
- [51] J. Bass and W. P. Pratt, Jr., *J. Phys.: Condens. Matter* **19**, 183201 (2007).
- [52] M. Gradhand, D. V. Fedorov, P. Zahn, and I. Mertig, *Phys. Rev. B* **81**, 245109 (2010).
- [53] Y. Niimi, D. Wei, H. Idzuchi, T. Wakamura, T. Kato, and Y. Otani, *Phys. Rev. Lett.* **110**, 016805 (2013).
- [54] The use of Eq. (2) implies we are using the same units for the spin Hall conductivity as for the longitudinal conductivity, following Ref. [29]. This is in contrast to some literature where definitions in units of \hbar/e [59] or $\hbar/(2e)$ [30,60] have been used. A discussion of this can be found in Ref. [55]. Accordingly, we have to divide the results in Refs. [30,60] by 2 to compare them to our results in the following.
- [55] D. V. Fedorov, C. Herschbach, A. Johansson, S. Ostanin, I. Mertig, M. Gradhand, K. Chadova, D. Ködderitzsch, and H. Ebert, *Phys. Rev. B* **88**, 085116 (2013).
- [56] We extract the shunting factor for each of our devices by considering their specific dimensions and resistivities and using the SPINFLOW 3D software [34]. Note that x_{Pt} is extremely sensitive to the geometrical parameters of the Cu and Pt wires. In a previous paper by some of the authors that reported SHE in Pt [24], x_{Pt} was obtained experimentally using an additional control sample. Due to a small difference in the width of the Pt and Cu wires between the studied devices and the control sample, x_{Pt} was overestimated, giving rise to an underestimation in σ_{SH} , ρ_{SH} , and θ_{SH} .
- [57] A. Fert and P. M. Levy, *Phys. Rev. Lett.* **106**, 157208 (2011).
- [58] S. Lowitzer, M. Gradhand, D. Ködderitzsch, D. V. Fedorov, I. Mertig, and H. Ebert, *Phys. Rev. Lett.* **106**, 056601 (2011).
- [59] T. Tanaka, H. Kontani, M. Naito, T. Naito, D. S. Hirashima, K. Yamada, and J. Inoue, *Phys. Rev. B* **77**, 165117 (2008).
- [60] L. Wang, R. J. H. Wesselink, Y. Liu, Z. Yuan, K. Xia, and P. J. Kelly, *Phys. Rev. Lett.* **116**, 196602 (2016).